Kinematics of Self-Centering Steel Plate Shear Walls with NewZ-BREAKSS Post-Tensioned Rocking Connection

DANIEL M. DOWDEN and MICHEL BRUNEAU

ABSTRACT

This paper presents information on the combined contribution of post-tensioning and beam-to-column joint rocking connections in self-centering steel plate shear walls (SC-SPSWs) with the NewZ-BREAKSS connection (i.e., NZ-SC-SPSW). Detailed free-body diagrams developed and presented in this paper provide insights on the basic, fundamental kinematic behavior of this lateral force-resisting system. The fundamental equations presented provide information on the behavior of SC-SPSWs and are suitable to facilitate design. These are needed for the implementation and understanding of these types of self-centering steel frame systems.

Keywords: rocking connection; self-centering; steel plate shear wall; moment frame; seismic response; resilient structure; seismic performance.

INTRODUCTION

Conventional steel lateral force-resisting systems (LFRSs) that comply with current building codes and the AISC seismic provisions (AISC, 2010) used in the United States are typically expected to suffer damage during moderate to severe earthquakes. Designed in accordance with prescribed detailing requirements proven by research to ensure ductile response (and protect occupants), these structural systems are not expected to collapse during a severe earthquake but will likely require significant repairs following a design level earthquake. Furthermore, the structure could be left with significant residual drifts and visible leaning following the earthquake (AIJ, 1995; Krawinkler et al., 1996; Kawashima et al., 1998; Christopoulos et al., 2003; Pampanin et al., 2003). Thus, although current conventional LFRSs can meet the code-specified objective of collapse prevention for standard buildings, significant structural damage occurs (albeit controlled damage), preventing use of the building for a significant repair period after a design level earthquake and possibly leading to demolition of the building in some cases. This seismic performance is typically expected for conventional LFRSs of any material and construction.

Recent research (Winkley, 2011; Clayton, 2013; Dowden, 2014) on self-centering steel plate shear walls (SC-SPSWs) has demonstrated that structures can be designed to achieve greater performance objectives by providing frame recentering capabilities after a seismic event, together with replaceable, energy-dissipating components. This self-centering capability in SPSWs is achieved here by using beam-to-column post-tensioned (PT) moment rocking frame connections, similar to what was done in past research on self-centering moment frames (e.g., Ricles et al., 2002; Christopoulos et al., 2002; Garlock et al., 2005; Rojas et al., 2005). However, to be fully successful, such self-centering strategies need to account for the interaction (due to the PT boundary frame expansion) between the LFRS and the gravity frame. Because self-centering buildings could economically provide a level of protection designated as available for "immediate occupancy" following an earthquake, this design strategy makes sense from a life-cycle cost perspective.

Toward that goal, this paper presents information on the analytical modeling and kinematics of a SC-SPSW with the proposed NewZ-BREAKSS (NZ) rocking connection (Dowden and Bruneau, 2011), a beam-to-column joint detail inspired by a moment-resisting connection developed and implemented in New Zealand (Clifton, 1996, 2005; Clifton et al., 2007; MacRae et al., 2008). This PT beam-to-column (i.e., horizontal boundary element–to–vertical boundary element, or HBE-to-VBE) rocking connection seeks to eliminate PT boundary frame expansion (i.e., beam

Daniel M. Dowden, Research Engineer, Structural Engineering and Earthquake Simulation Laboratory, Department of Civil, Structural, and Environmental Engineering, University at Buffalo, University at Buffalo, Buffalo, NY (corresponding). Email: dmdowden@buffalo.edu

Michel Bruneau, Professor, Department of Civil, Structural, and Environmental Engineering, University at Buffalo, University at Buffalo, Buffalo, NY. Email: bruneau@buffalo.edu

Paper No. 2015-23R

growth) that occurs in all the other previously researched rocking connections (referenced earlier). First, a review of the basic principles of the NZ-SC-SPSW is presented, from which equations for the moment, shear and axial force diagrams along the HBE are obtained from a capacity design approach based on yielding of the SPSW infill web plates. Using the derived equations, numerical models are then developed and results are compared with the closed-form analytical equations. Next, additional insight on the global force-displacement response of the NZ-SC-SPSW frame is provided through nonlinear monotonic pushover analyses. Furthermore, detailed free-body diagrams are developed to investigate infill web plate demands with frames with HBE-to-VBE rocking connections. Finally, insight on unrestrained PT boundary frame expansion of frames with HBE-to-VBE rocking connections gained from experiments (Dowden and Bruneau, 2014; Dowden et al., 2016) is provided, leading to an improved NewZ-BREAKSS detail.

BASIC PRINCIPLES OF THE NZ-SC-SPSW SYSTEM

An SC-SPSW differs from a conventional SPSW in that HBE-to-VBE rigid moment connections in a conventional SPSW are replaced by PT rocking moment connections. This allows a joint gap opening to form between the VBE and HBE interface about a rocking point, leading to a PT elongation, which is the self-centering mechanism. This particular rocking connection then eliminates PT boundary frame expansion typically encountered in the previously researched connections (that rock about both of their beam flanges) by, instead, maintaining constant contact of the HBE top flange with the VBEs during lateral drift. By doing so, when one of the rocking joint "opens," the rocking joint at the opposite end of the HBE "closes," as shown schematically in Figure 1a. As a result, the net gap opening (due to PT boundary frame expansion) is zero over the full length of the HBE. However, in this configuration, the PT elements require anchorage to the HBE, and while the PT at the opening joint will always contribute to frame recentering, the PT element at the closing joint may or may not, depending on the relationship between the initial PT force provided and the instantaneous frame drift.

A schematic of the NewZ-BREAKSS detail is shown in Figure 1b. In that figure, the connection detail includes an initial gap at the bottom of the HBE flanges, which allows rocking about the HBE top flanges only. As a result, during frame sway, an immediate increase and decrease of PT force occurs at the opening and closing joint locations, respectively. Compared to frames with HBE-to-VBE rocking joints that rock about both flanges (i.e., flange-rocking, or FR, connections), this results in a reduced PT boundary frame stiffness because, for FR connections, a delay in relative HBE-to-VBE gap opening occurs (because both top and bottom HBE flanges are initially in contact with the VBE). For frames detailed with FR connections, this frame type has the benefit that, at incipient initiation of joint gap opening (referred to as the condition when the "decompression-moment" strength of the joint is reached), the joint stiffness is comparable to that of a rigid-moment connection. Additionally, PT boundary frame stiffness softening also occurs with frames detailed with the NewZ-BREAKSS connection due to the relaxation of the PT elements at the closing joints during frame sway. However, scaled and full-scale tests (Dowden and Bruneau, 2014; Dowden et al., 2016) have shown that the absence of a decompression moment and relaxation of the PT elements at the closing joints do not have a detrimental effect on the response of NZ-SC-SPSWs.

Furthermore, the base connection of the VBEs for an SC-SPSW should be detailed such to allow free rotation without the formation of a plastic hinge mechanism (in contrast to conventional SPSWs, where a fixed VBE base connection is typically assumed). If a plastic hinge is able to form at the base of the VBE member, this could limit the self-centering potential of the PT boundary frame. Furthermore, providing a foundation detail free of damage would also use the SC-SPSW to its full potential. As a result, the only needed replaceable elements after a moderate or design level earthquake would be the infill web plates because all other elements are designed to remain essentially elastic.

Figure 1c shows the free-body diagram (FBD) of a NZ-SC-SPSW frame,

where

P_{S1} = PT axial compression force applied to the HBE at the gap opening joint

P_{S2} = PT axial compression force applied to the HBE at the gap closing joint

V_i = externally applied lateral forces at story i due to applied seismic forces

V_{BASE} = total base shear

M_{BASE} = total base overturning moment

ω = diagonal tension yield force developed by the steel web plates

All other terms have been previously defined. The diagonal tension yield forces of the web plate, ω, can be resolved into vertical and horizontal components on the VBE and HBE as provided in Equations 1 and 2 (Sabelli and Bruneau, 2007; Berman and Bruneau, 2008), respectively:

$$\omega_{cx} = F_{yp}t(\sin\alpha)^2 \qquad \omega_{cy} = \frac{F_{yp}t\sin 2\alpha}{2} \tag{1}$$

$$\omega_{bx} = \frac{F_{yp}t\sin 2\alpha}{2} \qquad \omega_{by} = F_{yp}t(\cos\alpha)^2 \tag{2}$$

where

w_{cx} and w_{cy} = horizontal and vertical components, respectively, along the height of the VBEs

w_{bx} and w_{by} = horizontal and vertical components, respectively, along the length of the HBEs

F_{yp} and t = yield stress and thickness of the web plate, respectively

α = angle of inclination of the diagonal tension field from the vertical axis, as typically calculated for SPSWs (AISC, 2010)

Here, forces shown on the FBD are taken assuming that the web plate thickness varies proportional to increasing story shears. Furthermore, the PT boundary frame is designed to essentially remain elastic, and hysteretic energy dissipation is intended to be provided by the infill web plates only.

The total hysteretic response of an NZ-SC-SPSW is provided by the combined elastic response of the PT boundary frame and the inelastic energy dissipation of the infill web plates. The idealized tension-only cyclic hysteretic response assuming a rigid boundary frame and an elastic-perfectly plastic hysteretic model of the infill web plates is shown in Figure 2. In particular, the PT boundary frame stiffness is bilinear elastic, where a reduced secondary PT boundary frame stiffness occurs when the PT at the closing joint becomes fully relaxed; analytical and experimental results (Dowden and Bruneau, 2014) show that this phenomenon has no significant detrimental effect on structural behavior and can be accommodated by design. Furthermore, past research has shown that solid infill web plates do not exhibit a tension-only behavior (as typically assumed for design), but some compression strength of the infill web plate develops due to the deformation of the infill web plate through tension field action (Winkley, 2011; Clayton, 2013; Webster, 2013; Dowden, 2014). However, recent research has also shown that, for dynamic earthquake loadings, this compression effect provides a slight amount of additional energy dissipation and strength but does not affect frame recentering (Dowden and Bruneau, 2014; Dowden et al., 2016).

HBE FREE-BODY-FORCE DIAGRAM

To understand the behavior of an NZ-SC-SPSW system, the moment, shear, and axial force diagrams for the HBE are first developed based on first principles. First, Figure 3 shows the general FBD of HBE and VBE elements located at an intermediate floor level of an SC-SPSW frame once the web plate has fully yielded, where W_{bx1}, W_{bx2} and W_{by1}, W_{by2} are, respectively, the horizontal and vertical force resultants

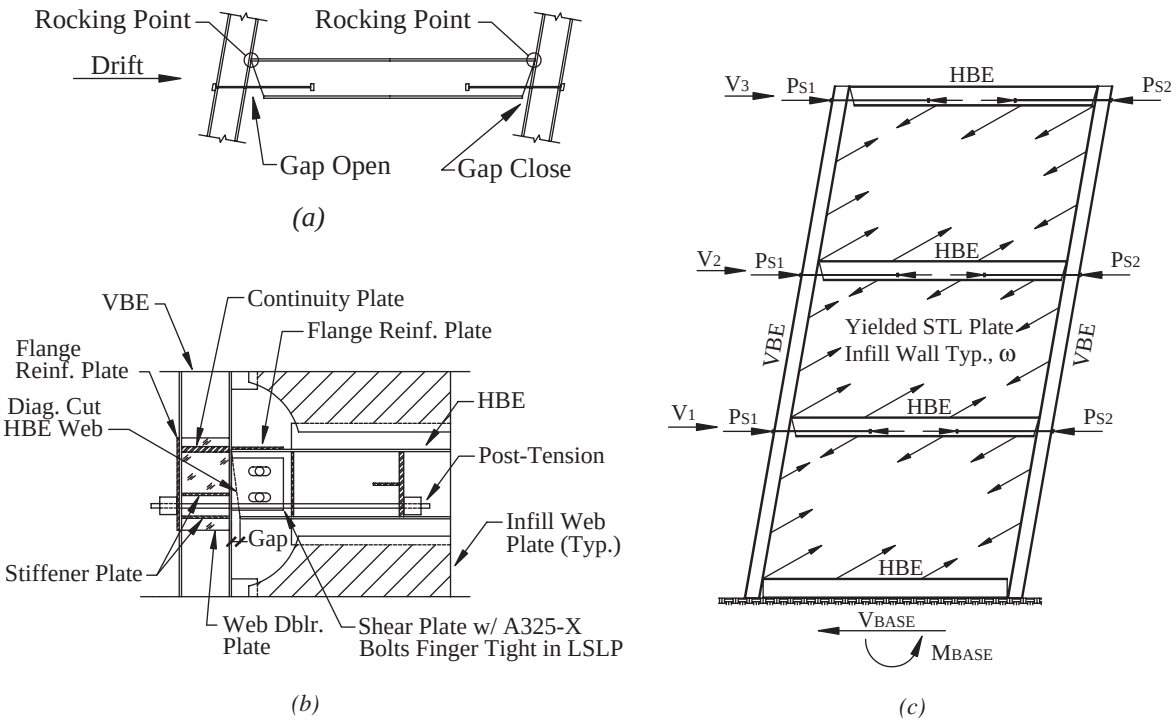

Fig. 1. NZ-SC-SPSW: (a) rocking joints; (b) rocking joint detail; (c) yield mechanism.

along the length of the HBE; W_{cx1}, W_{cx2} and W_{cy1}, W_{cy2} are, respectively, the horizontal and vertical force resultants along the height of the VBE; subscripts 1 and 2, respectively, denote the level below and above the HBE (here assuming that the force components labeled with subscript 1 are larger than subscript 2 associated with a thicker web plate below the HBE than above); H is the story height; and all other terms have been previously defined. Note that the vertical HBE end reactions would have to be resisted by a shear tab connection to the VBE (or equivalent); however, for clarity, the shear tab is not shown in the FBD illustrated.

Next, Figure 4 shows the resultant force FBD of an intermediate HBE for the condition shown in Figure 3 (neglecting gravity forces),

where

V_i = story shear force (as presented in Dowden et al., 2012, for the flange-rocking SC-SPSW) and is assumed to be equally distributed on each side of the frame

W_{bx} = infill web plate horizontal yield force resultant along the length of the HBE

W_{by} = infill web plate vertical yield force resultant along the length of the HBE

$P_{HBE(VBE)}$ = horizontal reaction at the rocking point of the yield force resultant of the infill web plate acting on the VBE (as presented in Sabelli and Bruneau, 2007)

P_s = PT force

P_{sVBE} = horizontal reaction of the post-tension force at the rocking point

R_1 = vertical reaction required for equilibrium of the vertical yield force component of the infill web plate along the HBE, as shown in Figure 5

R_2 = vertical reaction required for equilibrium of the horizontal yield force component of the infill web plate along the HBE, as shown in Figure 6

R_3 = vertical reaction required for equilibrium of the post-tensioned forces acting on the HBE, as shown in Figure 7

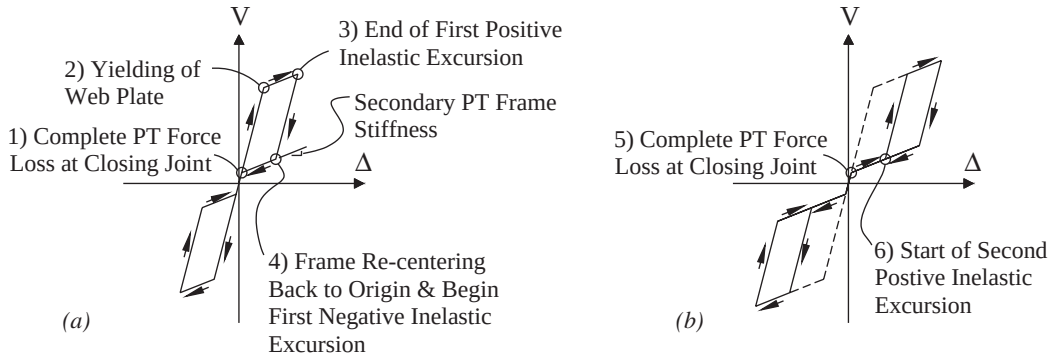

Fig. 2. Idealized hysteretic response of NZ-SC-SPSW: (a) cycle 1; (b) cycle 2.

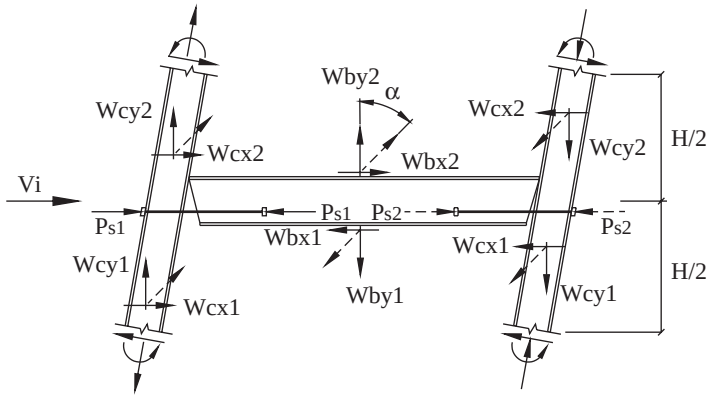

Fig. 3. Resultant force free-body diagram.

y = distance from the HBE neutral axis to the centroid of the PT

d = depth of the HBE

R = length of the radius corner cutout of the infill plate and represents the length of the end segments of the HBEs where the infill web plate is not attached as shown in Figure 1b (and will be further addressed subsequently)

L_1 = length of the HBE that corresponds to the HBE-to-VBE rocking point to the location of the post-tension anchor at the "opening joint" end of the HBE

L_2 = length of the HBE that corresponds to the HBE-to-VBE rocking point to the location of the post-tension anchor at the "closing joint" end of the HBE

L = clear span of the HBE. Also, it is assumed that the boundary frame and PT remain elastic and only the infill web plate yields

Furthermore, in Figure 4, the location of the PT anchor point along the beam will depend on the strain demands of the PT elements at the maximum target drift. The anchor location should be provided such to ensure that the PT strains remain elastic up to that drift demand. Additionally, to clarify the effects of P_{s1} and P_{s2}, each P_s component is composed of two forces: the initial post-tension force P_o, applied prior to drift and the force induced due to post-tension elongation during building drift, ΔP. For the condition shown, from geometry, elongation of post-tension will occur in P_{s1} while "relaxation" of the post-tension element P_{s2} will occur (for reasons described earlier), resulting in the following post-tension forces on the HBE:

$$P_{s1} = P_o + \Delta P = P_o + \frac{A_{PT1}E_{PT1}}{L_{PT1}}\left(\Delta_{drift} - \Delta_{loss}\right) \qquad (3)$$

$$P_{s2} = P_o - \Delta P = P_o - \frac{A_{PT2}E_{PT2}}{L_{PT2}}\left(\Delta_{drift} + \Delta_{loss}\right) \qquad (4)$$

Here, the subscripts 1 and 2 refer to the equation variables located on the HBE segment at the opening and closing joint, respectively, and

L_{PT} = length of the post-tension elements

A_{PT} = area of post-tension

E_{PT} = modulus of elasticity of the post-tension

Δ_{loss} = axial shortening that occurs along the HBE span length between the end of the HBE to the post-tension anchor point locations on the HBE

Δ_{drift} = drift-induced elongation of the post-tension elements at the HBE-to-VBE joint connection producing the incremental force ΔP, calculated as:

$$\Delta_{drift} = \phi_{drift}\left(\frac{d}{2} + y\right) \qquad (5)$$

where ϕ_{drift} is the relative HBE-to-VBE joint rotation in units of radians, and all other terms have been defined previously. From Equations 3 and 4, for a given lateral frame drift, an increase in force P_{s1} results in a simultaneous decrease in force of P_{s2} (and vice versa for lateral drift in the opposite direction). Additionally, if the force ΔP equals P_o, P_{s2} will become fully "relaxed," and this force component will vanish. In other words, for the condition when Δ_{net} (i.e., Δ_{drift} less Δ_{loss}) is equal to or greater than Δ_o, P_{s2} will equal zero. Consequently, the effectiveness of P_{s2} depends on the amount of initial post-tension force P_o as well as the maximum drift reached.

To calculate the loss in post-tension force from HBE axial shortening, using the PT located at the opening joint location to illustrate (as that condition will govern the PT design), equilibrium of axial forces in the post-tension elements requires that the increase in tension forces in the

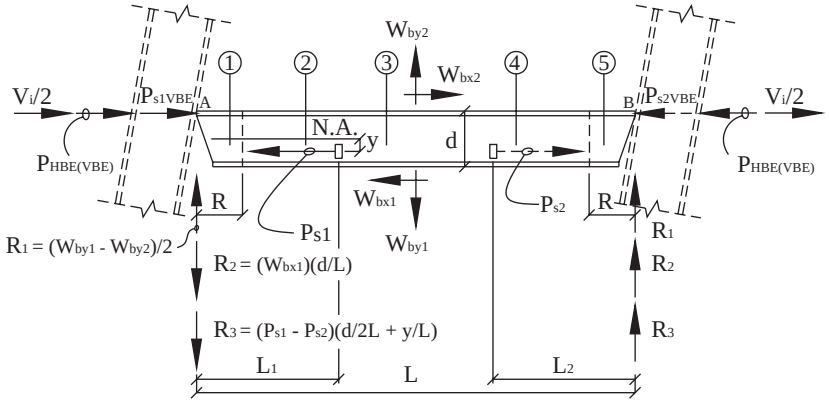

Fig. 4. Complete force-resultant free-body diagram of HBE.

post-tension elements equals the increase in compressive forces on the HBE (Garlock, 2002). For SC-SPSW systems, for equal story force at each end of the HBE (i.e., $V_i/2$ each end of the SC-SPSW frame), the post-tension force losses are attributed to the HBE axial shortening under the axial compression force from the VBE and the axial compression force due to the post-tension elongation during lateral drift (with the simplified assumption of rigid VBEs). Furthermore, the PT force contributing to HBE axial shortening along the length of the HBEs between PT anchor points, is a smaller fractional value of the tension force in the PT elements; a schematic of this is illustrated in Figure 8. The calculation of PT force losses due to HBE axial shortening then follows:

$$\Delta_{loss} = \frac{(P_{PT} \times SF) L_1}{A_{HBE} E_{HBE}} + \frac{P_{HBE(VBE)} L_1}{A_{HBE} E_{HBE}} \tag{6}$$

where

SF = some scale factor (presented subsequently)

P_{PT} = force in the post-tension element (i.e., P_{s1})

A_{HBE} = cross-section area of the HBE

E_{HBE} = modulus of elasticity of the HBE

All other terms have been previously defined. Next, solving Equation 6 for P_{PT} leads to the following:

$$P_{PT} = \frac{1}{SF}\left(\frac{A_{HBE} E_{HBE}}{L_1} \Delta_{loss} - P_{HBE(VBE)}\right) \tag{7}$$

Correspondingly, the net effective axial tension force in the post-tension elements is the elongation due to drift minus the axial shortening of the HBE that occurs along the length of the post-tension elements and is calculated as follows:

$$P_{PT} = \left(\frac{A_{PT} E_{PT}}{L_{PT}}\right)\left(\Delta_{drift} - \Delta_{loss}\right) = k_{PT}\left(\Delta_{drift} - \Delta_{loss}\right) \tag{8}$$

Next, equating Equations 7 and 8, then solving for Δ_{loss}, leads to the amount of post-tension relaxation that should be considered for design and is calculated as:

$$\Delta_{loss} = \frac{P_{HBE(VBE)}}{k^*_{PT} + \dfrac{A_{HBE} E_{HBE}}{L_1}} + \left(\frac{k^*_{PT}}{k^*_{PT} + \dfrac{A_{HBE} E_{HBE}}{L_1}}\right)\Delta_{drift} \tag{9}$$

where the SF and the post-tension axial stiffness terms have been combined such that:

$$k^*_{PT} = \left(\frac{A_{PT} E_{PT}}{L_{PT}}\right) SF = (k_{PT})(SF) \tag{10}$$

and, from Figure 8, the scale factor can be approximated as:

$$SF = \left(\frac{h - y}{h + 0.5d}\right) \tag{11}$$

where

h = distance from the bottom of the VBE to the centroid of the HBE

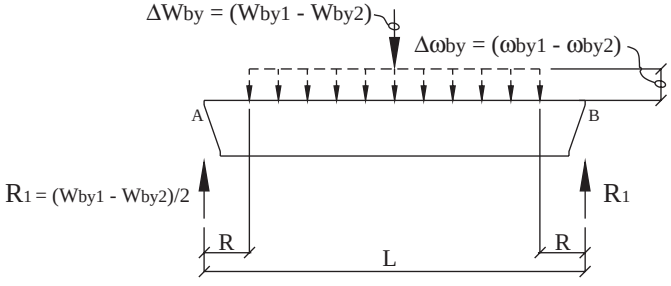

Fig. 5. Free-body diagram vertical component.

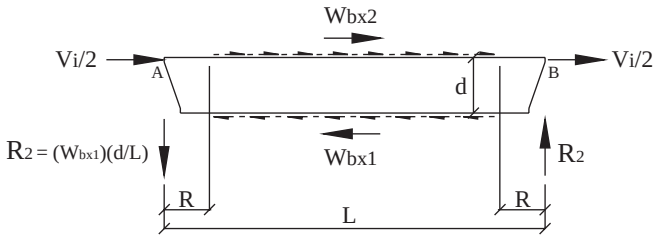

Fig. 6. Partial free-body diagram horizontal component.

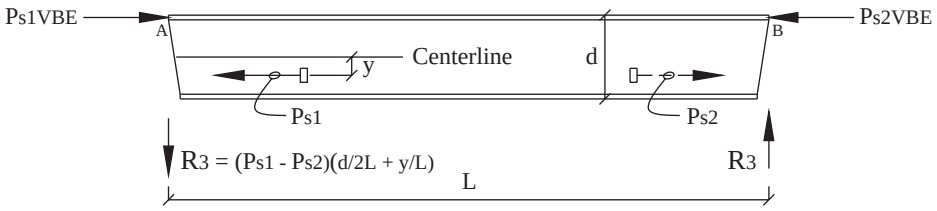

Fig. 7. Free-body diagram post-tension forces.

y = distance of the PT from the HBE centroid

d = depth of the HBE

Finally, the resulting equations for P_s, for the rightward drift condition shown in Figure 1c, which includes losses due to HBE axial shortening, is obtained by substituting Equation 9 into Equations 3 and 4, leading to:

$$P_{s1} = P_o + \left(\frac{k_{b1}k_{PT}^*}{k_{b1}+k_{PT}^*}\right)\Delta_{drift} - \frac{k_{PT}^*}{k_{b1}+k_{PT}^*}P_{HBE(VBE)} \quad (12)$$

$$P_{s2} = P_o - \left(\frac{k_{b2}k_{PT}^* + 2\left(k_{PT}^*\right)^2}{k_{b2}+k_{PT}^*}\right)\Delta_{drift} - \frac{k_{PT}^*}{k_{b2}+k_{PT}^*}P_{HBE(VBE)} \quad (13)$$

where, in Equations 12 and 13, k_{b1} and k_{b2} are the HBE axial stiffness along length L_1 and L_2, respectively.

Development of HBE Moments

The moment distribution to be used in the design of an HBE incorporating self-centering components can be determined from the free-body diagram of Figure 4. As indicated in that figure, five locations along the HBE are considered: the two segments of HBE where the infill web plate is cut out (thus not connected to the HBE flange), the two segments of the HBE between the infill web plate corner cutout and the post-tension anchor point, and the segment of the HBE between the post-tension anchor points along the length of the HBE. These locations, for the purpose of presentation, are designated as zone 1, zone 2, zone 3, zone 4, and zone 5. The FBD for zone 1 is shown in Figure 9.

Furthermore, for illustration purposes, in Figure 9 the horizontal compression reaction at the HBE-to-VBE flange rocking point and vertical HBE end reaction (components shown in Figure 4) are combined into a single variable C and R_A, respectively. The determination of the HBE flexural strength demand then follows by taking moment equilibrium at the HBE section cut 1; the moment relationship in terms of force resultants is:

$$M_1 = R_a x + C\left(\frac{d}{2}\right) \quad (14)$$

Substituting Equations 1 and 2, along with the equivalent force per unit length quantities for the resultant forces defined earlier, into Equation 14, the resulting moment relationship expressed in terms of the infill web plate yield forces per unit length along the HBE along zone 1 is:

$$\begin{aligned} M_1 = {} & P_{s1(VBE)}\left(\frac{d}{2}\right) - P_{s1}\left(\frac{d}{2L}x + \frac{y}{L}x\right) + P_{s2}\left(\frac{y}{L}x + \frac{d}{2L}x\right) \\ & + \left(\omega_{by1} - \omega_{by2}\right)\left(\frac{L}{2}x - Rx\right) \\ & + \left(\omega_{cx1} + \omega_{cx2}\right)\left(\frac{dh}{4} - \frac{d^2}{4} - \frac{dR}{2}\right) \\ & + \omega_{bx1}\left(\frac{2dR}{L}x - dx\right) + V_i\left(\frac{d}{4}\right) \end{aligned} \quad (15)$$

Similarly, by moment equilibrium at the remaining sections 2 through 5, the moment distribution along these zones is:

$$\begin{aligned} M_2 = {} & P_{s1(VBE)}\left(\frac{d}{2}\right) - P_{s1}\left(\frac{d}{2L}x + \frac{y}{L}x\right) + P_{s2}\left(\frac{y}{L}x + \frac{d}{2L}x\right) \\ & + \left(\omega_{by1} - \omega_{by2}\right)\left(\frac{L}{2}x - \frac{x^2}{2} - \frac{R^2}{2}\right) + \left(\omega_{cx1} + \omega_{cx2}\right)\left(\frac{dh}{4} - \frac{d^2}{4} - \frac{dR}{2}\right) \\ & + \omega_{bx1}\left(\frac{2dR}{L}x - \frac{d}{2}x - \frac{dR}{2}\right) + \omega_{bx2}\left(\frac{d}{2}x - \frac{dR}{2}\right) + V_i\left(\frac{d}{4}\right) \end{aligned} \quad (16)$$

$$\begin{aligned} M_3 = {} & P_{s1(VBE)}\left(\frac{d}{2}\right) + P_{s1}\left(y - \frac{d}{2L}x - \frac{y}{L}x\right) + P_{s2}\left(\frac{y}{L}x + \frac{d}{2L}x\right) \\ & + \left(\omega_{by1} - \omega_{by2}\right)\left(\frac{L}{2}x - \frac{x^2}{2} - \frac{R^2}{2}\right) + \left(\omega_{cx1} + \omega_{cx2}\right)\left(\frac{dh}{4} - \frac{d^2}{4} - \frac{dR}{2}\right) \\ & + \omega_{bx1}\left(\frac{2dR}{L}x - \frac{d}{2}x - \frac{dR}{2}\right) + \omega_{bx2}\left(\frac{d}{2}x - \frac{dR}{2}\right) + V_i\left(\frac{d}{4}\right) \end{aligned} \quad (17)$$

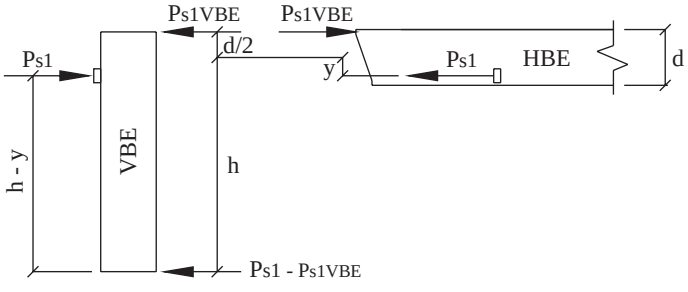

Fig. 8. Reduced post-tension force on HBE.

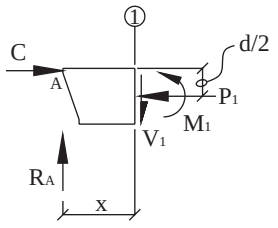

Fig. 9. Free-body diagram along zone 1.

$$M_4 = P_{s1VBE}\left(\frac{d}{2}\right) + P_{s1}\left(y - \frac{d}{2L}x - \frac{y}{L}x\right) + P_{s2}\left(\frac{y}{L}x + \frac{d}{2L}x - y\right) + \left(\omega_{by1} - \omega_{by2}\right)\left(\frac{L}{2}x - \frac{x^2}{2} - \frac{R^2}{2}\right) + \left(\omega_{cx1} + \omega_{cx2}\right)\left(\frac{dh}{4} - \frac{d^2}{4} - \frac{dR}{2}\right) + \omega_{bx1}\left(\frac{2dR}{L}x - \frac{d}{2}x - \frac{dR}{2}\right) + \omega_{bx2}\left(\frac{d}{2}x - \frac{dR}{2}\right) + V_i\left(\frac{d}{4}\right) \quad (18)$$

$$M_5 = P_{s1(VBE)}\left(\frac{d}{2}\right) + P_{s1}\left(y - \frac{d}{2L}x - \frac{y}{L}x\right) + P_{s2}\left(\frac{y}{L}x + \frac{d}{2L}x - y\right) + \left(\omega_{by1} - \omega_{by2}\right)\left(\frac{L^2}{2} + Rx - \frac{L}{2}x - LR\right) + \left(\omega_{cx1} + \omega_{cx2}\right)\left(\frac{dh}{4} - \frac{d^2}{4} - \frac{dR}{2}\right) + \omega_{bx1}\left(\frac{2dR}{L}x - dx + \frac{dL}{2} - dR\right) + \omega_{bx2}\left(\frac{dL}{2} - dR\right) + V_i\left(\frac{d}{4}\right) \quad (19)$$

Development of HBE Shear and Axial Forces

The shear distribution to be used in the design of an HBE can be determined using the same FBD and procedure as presented earlier, which then leads to:

$$V_1 = R_a = \frac{\left(\omega_{by1} - \omega_{by2}\right)(L - 2R)}{2} - \frac{(\omega_{bx1})(L - 2R)}{L}d - (P_{s1} - P_{s2})\left(\frac{d}{2L} + \frac{y}{L}\right) \quad (20)$$

$$V_2 = V_3 = V_4 = R_a - \left(\omega_{by1} - \omega_{by2}\right)(x - R) \quad (21)$$

$$V_5 = R_a - \left(\omega_{by1} - \omega_{by2}\right)(L - 2R) \quad (22)$$

Similarly, for axial forces over each of the five zones:

$$P_1 = C = \frac{\left(\omega_{bx1} - \omega_{bx2}\right)(L - 2R)}{2} + \left(\omega_{cx1} + \omega_{cx1}\right)\left(\frac{h}{2} - \frac{d}{2} - R\right) + P_{s1(VBE)} \quad (23)$$

$$P_2 = C - \left(\omega_{bx1} - \omega_{bx2}\right)(x - R) \quad (24)$$

$$P_3 = C - \left(\omega_{bx1} - \omega_{bx2}\right)(x - R) - \left(P_{s1} + P_{s2}\right) \quad (25)$$

$$P_4 = C - \left(\omega_{bx1} - \omega_{bx2}\right)(x - R) \quad (26)$$

$$P_5 = C - \left(\omega_{bx1} - \omega_{bx2}\right)(L - 2R) \quad (27)$$

Note that the development of the HBE moment, shear, and axial force formulations presented are based on a capacity design approach where the web plates have fully yielded. Consideration of PT force losses due to HBE elastic axial shortening has been considered. However, some vertical deflection of the HBE will occur due to the vertical component of the infill web plate tension forces pulling on the HBE. This results in HBE-to-VBE rotational components that will have an influence on the actual joint gap opening/closing, thus affecting the axial elongation response of the PT elements. However, this contribution of joint gap response can be neglected, without significant loss in accuracy, as will be observed in the following section. But to precisely account for this effect, a nonlinear pushover analysis would be needed. Furthermore, the derivations of the closed-form equations presented for the HBE strength demands assume rigid VBEs. In particular, the contribution of the flexibility of the VBEs contributing to PT force losses is neglected. Consideration of VBE flexibility can be included in a nonlinear pushover analysis once the numerical model is established (for which the equations presented earlier can be used to facilitate the initial design). Finally, as shown in Figure 4, Equations 14 through 27 were derived with the assumption that the story force (i.e., V_i) is equally distributed on each side of the frame. For the condition when the story force is delivered to only one side of the frame, Figure 6 would be modified to show V_i acting at location A and $V_i = 0$ at location B in that figure (note that the value of the reaction R_2 shown in that figure would remain unchanged). This would have the effect of increasing the HBE moment and axial force demand proportionally to V_i versus $V_i/2$.

NUMERICAL MODEL COMPARISON

The formulations describing the distribution of moment, shear and axial forces developed earlier were compared to results from nonlinear pushover analysis conducted using SAP2000 (CSI, 2009). Additionally, numerical modeling in OpenSees (Mazzoni et al., 2009) is also presented subsequently for reference. The example SPSW used for this purpose consisted of a single-bay, single-story frame with a bay width of 20 feet and story height of 10 feet. The SPSW web plate consisted of a 16-gauge infill light-gauge plate. A total of eight ½-in.-diameter, Grade 270 ksi steel monostrands were provided at each end of the HBE with a distance of 6 in. below the neutral axis of the HBE to the centroid of the tendons. An initial post-tensioning force of approximately 20% of the yield strength of the PT was provided. The depth of the HBE was taken to be 18 in., corresponding to a W18 beam.

Furthermore, a strip model was used for the infill web plate (Sabelli and Bruneau, 2007), as shown in Figure 10. Accordingly, because the hysteretic behavior of SPSWs relies on yielding of the infill web plate through diagonal tension field action, the infill web plate was conservatively

modeled by using a series of tension-only strips. Each of the strips was assigned an axial plastic hinge model to account for nonlinear hysteretic behavior. The PT boundary frame and post-tension elements were designed to remain elastic.

For the rocking connection in SAP2000, a rigid-beam element was used as a link to model the post-tension anchor points to the HBE to capture the applied moment during rocking motion about the HBE centerline. Joint constraints in the translational vertical global degrees-of-freedom (DOF) and in-plane (HBE strong axis bending) rotational DOF were provided at key nodes. For the case of modeling in OpenSees, rigid-link beams are used in lieu of joint constraints (with the exception of modeling the HBE to VBE shear transfer). The connection models for use in SAP2000 and OpenSees are shown in Figure 11.

For the current example, the designed SPSW is used to avoid abstract complexities in keeping the problem parametric. Additionally, the boundary frame members are assumed rigid here such that PT force losses due to HBE axial shortening can be ignored because this has a negligible impact on the results and keeps the conceptual illustration manageable. The formulations developed earlier are applicable regardless of whether PT force losses are considered. Only the P_{s1} and P_{s2} terms in the equations are affected and would need to include the PT force losses as presented in Equations 12 and 13. Figure 12 provides comparisons of the moment, shear and axial force distributions along the length of the HBE using the formulations developed earlier to those with the numerical model of the SAP2000 analysis for a rightward 3% drift condition. Note that because the SAP2000 model uses a finite number of strips to represent the infill web plate, the shear and axial force diagrams obtained from the

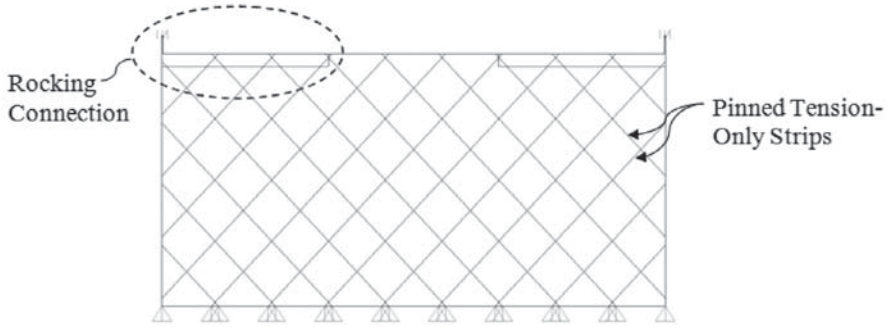

Fig. 10. NZ-SC-SPSW model.

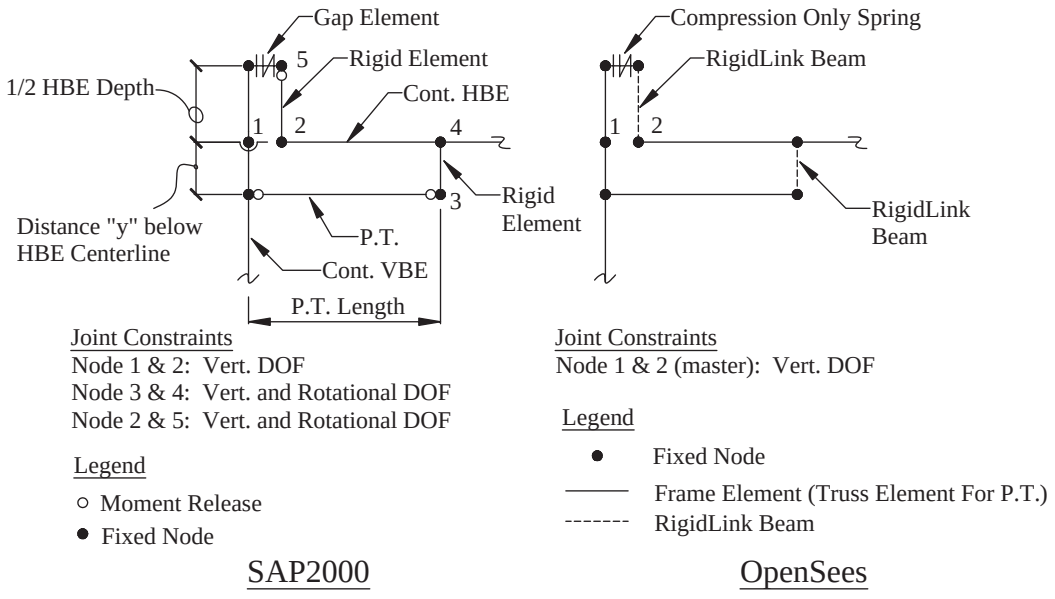

Fig. 11. NewZ-BREAKSS connection model.

SAP2000 analysis are stepped as compared to the continuous force diagrams using the analytical formulations.

Furthermore, the analytical formulations are compared to two different SAP2000 curves labeled "actual" and "idealized," where, for the condition of a rigid HBE, the idealized curve matches the analytical one almost perfectly for the moment and shear diagrams. The difference between the two different numerical models is that the idealized curves assume a pinned connection at the HBE-to-VBE flange contact rocking point. This represents the idealized condition assumed in the development of the equations presented previously. The actual model uses the compression-only element shown in Figure 11, which models more accurately the real condition of the joint detail. To further clarify, the preceding derivations assume that the effects on the post-tension (i.e., terms P_{s1} and P_{s2}) are exactly equal; which is essentially true for the rigid HBE condition if the HBE is pin connected to the VBEs. However, with the use of the compression-only element, some differences arise in response because now the compression force at the closing joint can be reduced (from the global effects captured by the numerical frame model that is not considered in the analytical formulations), leading to small differences in the kinematics governing the axial tension in the post-tension elements. It is also observed that on the SAP2000 moment and axial diagram curves, the post-tension force at the closing joint has not fully relaxed because there is a vertical step in the response curves. The results from the SAP2000 analysis and the corresponding analytical formulations compare reasonably along the full length of the HBE.

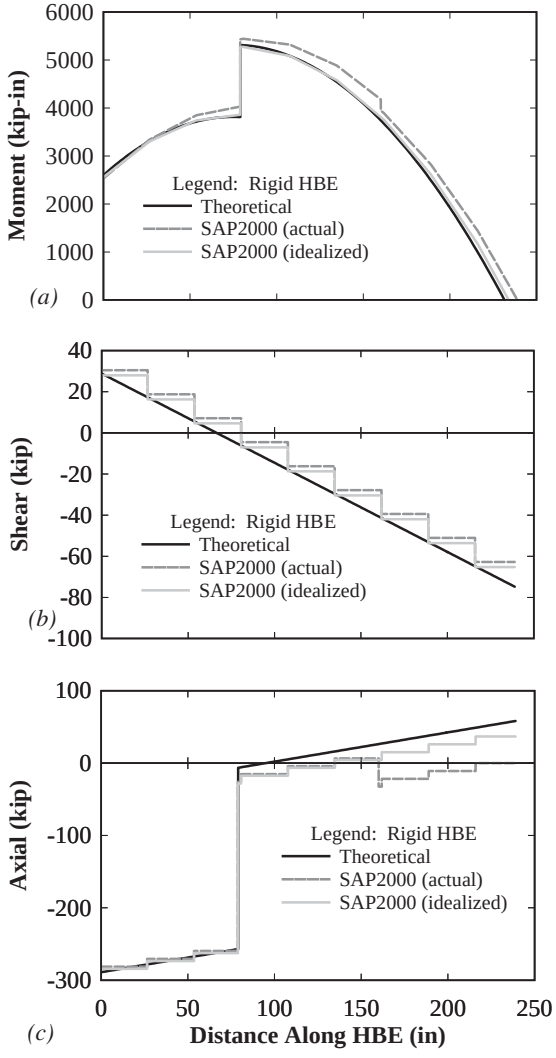

Fig. 12. SAP2000 nonlinear pushover analysis comparison.

To provide some comparison of numerical results using SAP2000 versus OpenSees, a nonlinear cyclic pushover analysis was conducted for the one-third-scale, single-bay, three-story NZ-SC-SPSW test frame investigated by Dowden and Bruneau (2014). The design parameters of the frame along with the corresponding numerical model are shown in Figure 13. Material properties consisted of ASTM A992, A416 and A1008 for the boundary frame, ½-in.-diameter PT monostrands, and infill web plate members, respectively. The VBE column bases were detailed with a clevis-and-pin base to allow free rotation, and all anchor connections to the foundation were bolted. To model the nonlinear hysteretic response of the infill web plates, nonlinear axial hinge assignments were used in the numerical model based on results from coupon testing. Additionally, an initial post-tensioning force of approximately 20% of the PT yield strength was used. The comparison of the base shear versus roof drift response obtained using the programs SAP2000 and OpenSees is shown in Figure 14; the results are practically identical.

POST-TENSION FORCE EFFECTS ON GLOBAL FRAME RESPONSE

A general base shear versus roof displacement response for the NZ-SC-SPSW was presented in Figure 2, where the contribution of the PT boundary frame response is observed to be bilinear elastic. To investigate the effects of various PT parameters on the response of the boundary frame, the variation in frame response when changing the initial PT force (T_o) and the quantity of PT strands (A_{PT}) is presented for the frame shown in Figure 13. In the following figures, response curves for the condition labeled 1xT_o and 1xA_{PT} correspond to the PT design parameters used in the test specimen (as a reference point). In this investigation, note that (1) all other design parameters (i.e., member sections, distance of PT eccentricity to the rocking point, etc.) remain the same because changing those would require other design changes, and (2) practical considerations of construction tolerances

are not considered because only the consequences of relative change in response are of interest here. Furthermore, this investigation is only made for the PT boundary frame, with the understanding that the total response is a superposition of the effects of the PT boundary frame and the infill web plate.

The variation in response due to T_o as the parametric variable is presented in Figure 15a, with A_{PT} held constant. Note that if significant PT yield occurs for a given T_o, no additional parametric curves are presented for that frame because only the elastic response of the boundary frame is of interest here (i.e., no yielding of PT elements, which would alter the frame response). It is observed that with T_o = 0 kips (i.e., 0xT_o), the frame response moves along a single elastic curve; thus, the presence of an initial PT force is what defines the bilinear frame response. Of particular interest, the location of the transition point between the initial and secondary stiffnesses is defined by the magnitude of T_o (as shown in Figure 2). More specifically, increasing the initial applied PT force results in (1) a positive shift of that transition point along the horizontal axis, resulting in an increase of the initial stiffness range of response that has the largest stiffness along the bilinear response curve, and (2) a positive shift of that transition point along the vertical axis, contributing more strength to the hysteretic response of the entire system.

The variation in response due to A_{PT} is presented in Figure 15b, with T_o held constant. In doing so, the quantity of PT strands (or rods) affects the stiffness (i.e., slopes) of the response curves (as would be expected). Furthermore, as A_{PT} increases, the effects of the secondary PT boundary frame stiffness (i.e., condition when T_o reduces to zero) become more dominant over the initial stiffness. This is due to a reduction in T_o in each corresponding PT strand (i.e., T_o remains constant; however, T_o per strand decreases proportional to the increase in A_{PT}). As a consequence, not only does increasing A_{PT} affect both initial and secondary stiffness of the PT boundary frame response curves, but increasing A_{PT} also shifts the transition point between the initial and secondary frame stiffness toward the axis origin (whereas increasing T_o shifts the transition point away). In comparison to Figure 15a, a significant increase in stiffness can be achieved without concern of yielding the PT elements for a target drift; however, it is at the expense of larger strength demands on the boundary frame than consideration of T_o alone.

INFILL WEB PLATE STRAINS EFFECTS DUE TO HBE-TO-VBE GAP OPENING

As presented earlier, radius corner cutouts are provided at the infill web plate corner locations. The primary purpose of this detail is to remove the portion of the infill web plate at the corner locations that would otherwise be subjected to excessive tensile strains during lateral frame drift due to the opening of the rocking joint (as schematically shown in Figure 16).

To determine the appropriate value of the radius corner cutout to use in design, a review of the kinematics of the joint detail under frame sway is necessary and is performed next,

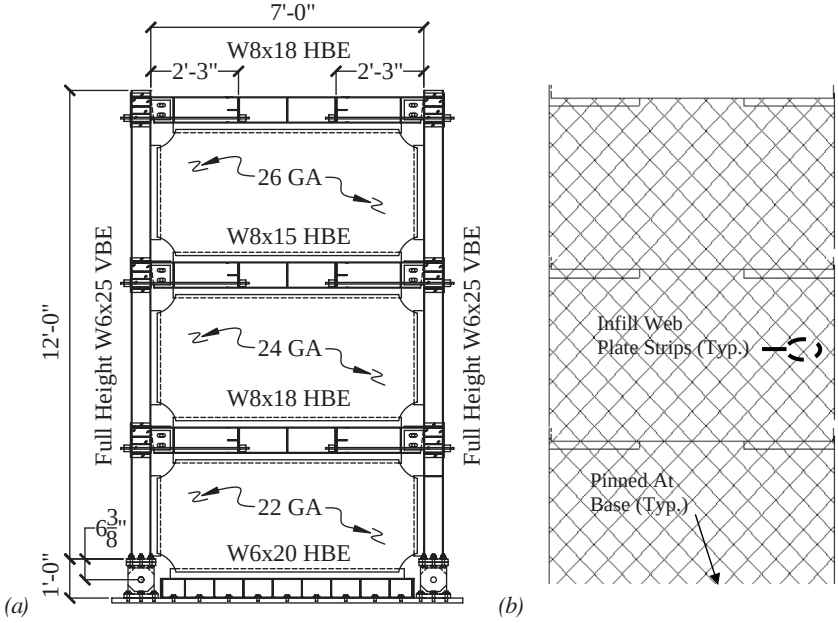

Fig. 13. (a) Frame parameters; (b) numerical model.

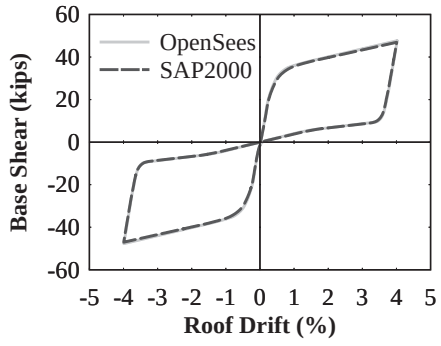

Fig. 14. Comparison of SAP2000 and OpenSees.

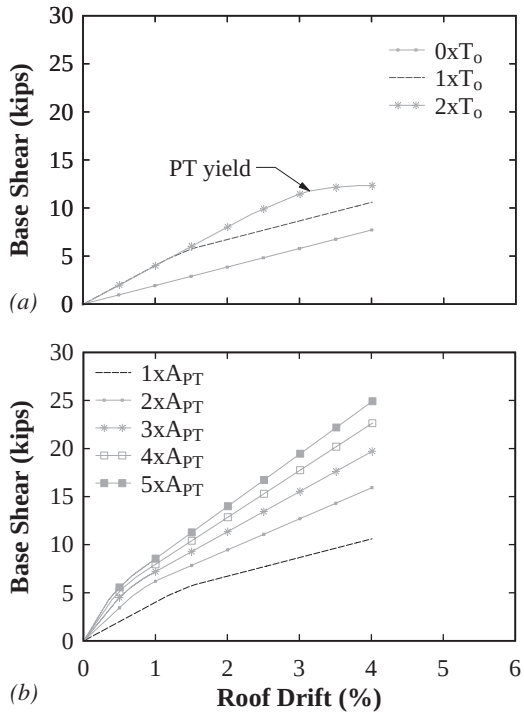

Fig. 15. PT boundary frame: (a) T_o variable; (b) A_{PT} variable.

based on small-angle theory. Figure 17 shows the geometry and parameters necessary to establish the kinematic relationships governing the infill web plate tensile strains when also including the HBE-to-VBE gap openings in the calculation of strains.

In Figure 17, R is the radius length of the corner cutout, L is the length of the adjacent infill web strip to the corner (shown idealized), α is the angle of inclination of the tension field to the vertical axis, ΔR are differential lengths dependent on the value α, Δgap is the HBE-to-VBE gap opening, d is the depth of the HBE, and γ is the gap opening rotation. To determine the total cumulative axial tensile strain of the strip adjacent to the tip of the radius cutout, the following relationships are established from geometry. The length L is obtained from the initial condition geometry (triangle 1-2-3) as:

$$L = \frac{R + \Delta R_1}{\sin\alpha} \tag{28}$$

Next, the axial tensile deformation of the infill web strip due to gap opening is (using the geometry of triangle 5-6-7):

$$\delta = \left(\Delta_{gap}\right)\cos(90 - \alpha) \tag{29}$$

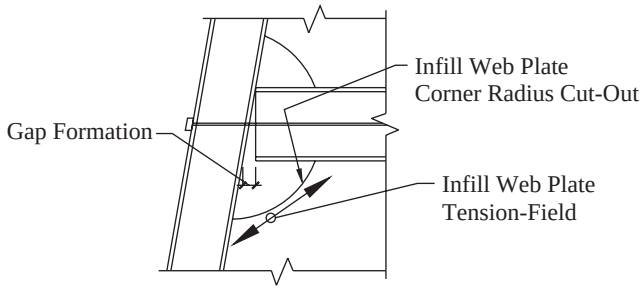

Fig. 16. HBE-to-VBE joint gap formation.

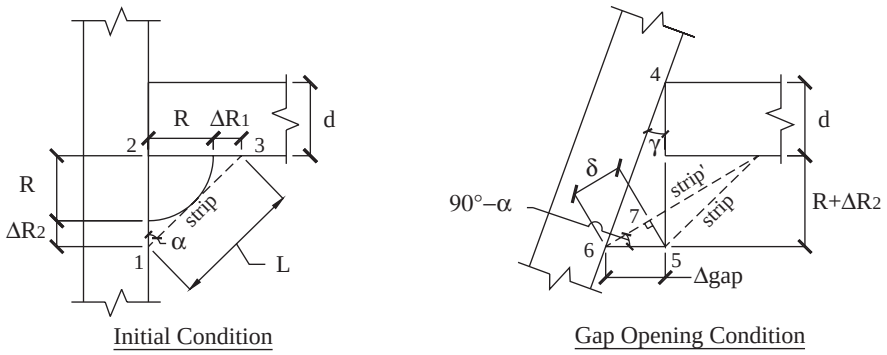

Fig. 17. HBE-to-VBE rocking joint kinematics.

The gap opening can then be calculated (using geometry of triangle 4-5-6) as:

$$\Delta_{gap} = \gamma\left(d + R + \Delta R_2\right) \tag{30}$$

It is also observed that (using the geometry of triangle 1-2-3):

$$\tan\alpha = \frac{\left(R + \Delta R_1\right)}{\left(R + \Delta R_2\right)} \tag{31}$$

Next, the differential term ΔR_2 is established (for reasons to be made clear subsequently). To proceed, Figure 18 shows the additional information needed to determine this quantity.

It then follows, using triangle 1 in Figure 18 and the sine double-angle identity, that the parameter $x1$ is:

$$x1 = R\sin(90 - \alpha) = R\cos\alpha \tag{32}$$

Furthermore, from the same triangle 1, the term $y1$ can be determined as follows:

$$y1 = R\sin\alpha \tag{33}$$

Next, from the geometry of triangle 2 in Figure 18, substituting Equation 32 for $x1$ and solving for $y2$ leads to:

$$y2 = \frac{R\cos\alpha}{\tan\alpha} \tag{34}$$

Furthermore, in Figure 18 it is observed that:

$$\Delta R_2 + R = y1 + y2 \tag{35}$$

which, substituting Equations 33 and 34 for $y1$ and $y2$, respectively, in Equation 35 and solving for ΔR_2, leads to:

$$\Delta R_2 = y1 + y2 - R = R\sin\alpha + \frac{R\cos\alpha}{\tan\alpha} - R \tag{36}$$

The resulting infill web plate tensile strain can then be expressed as:

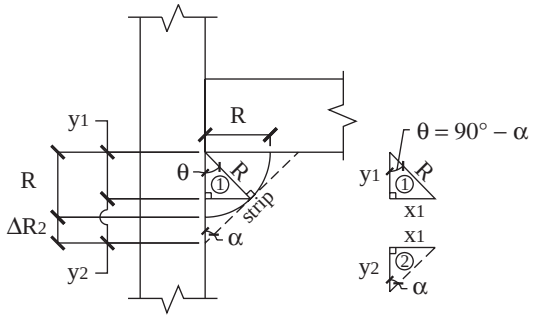

Fig. 18. Infill web plate corner cutout dimensions.

$$\varepsilon = \frac{\delta}{L} = \frac{\Delta_{gap}\sin\alpha}{\left(\dfrac{R + \Delta R_1}{\sin\alpha}\right)} \tag{37}$$

Substituting the terms for Δ_{gap} and $(R + \Delta R_1)$ using Equations 30 and 31 into Equation 37, it then follows that:

$$\varepsilon = \frac{\gamma\left(d + R + \Delta R_2\right)\sin^2\alpha}{\left(R + \Delta R_2\right)\tan\alpha} \tag{38}$$

Next, substituting ΔR_2 from Equation 36 and simplifying leads to:

$$\varepsilon = \frac{\gamma\left(d + \dfrac{R\cos\alpha}{\tan\alpha} + R\sin\alpha\right)\left(\sin\alpha\cos\alpha\right)}{R\left(\dfrac{\cos\alpha}{\tan\alpha} + \sin\alpha\right)} \tag{39}$$

Finally, Equation 39 can be further simplified by the substitution of the sine double-angle identity, which then results in the following expression:

$$\varepsilon_{Total} = \frac{\gamma\sin 2\alpha}{2}\left(\frac{\dfrac{d}{R}\tan\alpha + \cos\alpha + \sin\alpha\tan\alpha}{\cos\alpha + \sin\alpha\tan\alpha}\right) \tag{40}$$

Equation 40 represents the total tensile strain on the infill web plate for HBE-to-VBE rocking connections at a distance R away from the HBE-to-VBE flange rocking point. To further clarify the effects of Equation 40, for the case of $\alpha = 45$ degrees, Equation 40 results in the following:

$$\varepsilon_{Total} = Component1 + Component2 = \frac{\gamma d\sqrt{2}}{4R} + \frac{\gamma}{2} \tag{41}$$

where, in Equation 41, *Component*1 is the contribution of tensile strain from the gap opening and *Component*2 is the contribution from lateral frame drift (i.e., a rigid panel sway mechanism). To further illustrate, Figure 19a shows the axial strain demand for several different lateral drift conditions. From the results shown, the closer the infill web plate is to the corner (corresponding to a smaller R), the larger the strain demands. In particular, if $R = 0$, the theoretical strain is infinite.

Furthermore, Figure 19b shows the total axial tensile strain, together with the strain corresponding to each component, for a 2% drift condition. From the results shown, the concentration of strains in the infill web plate due to the use of a rocking connection is a localized phenomenon, with values approaching those for the rigid-panel sway mechanism away from the rocking connection gap opening. Note that in the examples presented, the gap rotation was assumed to be equal to the drift rotation, which assumes rigid sway

behavior as an approximation; a more exact joint rotation could be obtained from a rigorous frame analysis. Nonetheless, the preceding equations provide an approach to select the radius of the corner cutouts. As an example, SC-SPSW test specimens investigated by Dowden and Bruneau (2014) were detailed with an R/d ratio of approximately 1. For this condition shown in Figure 19a (i.e., $\alpha = 45$ degrees), for the case of 2% roof drift, Equation 40 predicts a maximum theoretical infill web plate tensile strain of approximately 1.7%. In particular, from observations of the experimental results presented by Dowden and Bruneau (2014), infill web plate separation from the boundary frame started to develop at approximately 2% roof drift (a drift magnitude expected for a design level earthquake), propagating from the plate corners. This provides some indication that the R/d ratio of 1.0 used in the HBE-to-VBE joint detail for the infill web plate corners performed reasonably well to delay the effects of initial web plate tearing from the boundary frame.

Finally, note that the preceding strain equations are applicable to any HBE-to-VBE joint rocking configuration because only the distance from the rocking contact point to the HBE flange needs to be modified in the equations presented. For example, for a centerline-rocking frame (Dowden and Bruneau, 2014), $d/2$ (half-depth of the HBE) would be used in lieu of d in the equations, and for the NewZ-BREAKSS and flange-rocking (Clayton et al., 2012; Dowden et al., 2012) connections, no changes to the equations presented are required because both connections follow the same kinematics at the opening joints when the HBE-to-VBE gap is present.

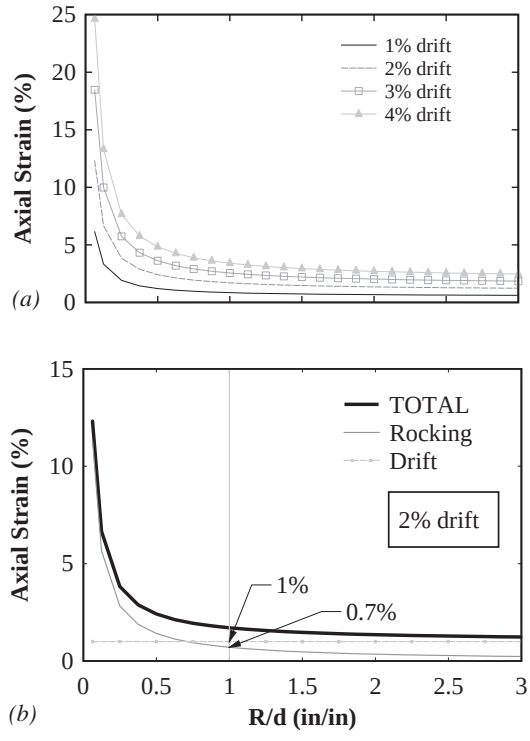

Fig. 19. Corner infill web plate: (a) strain demands; (b) strain components.

PT BOUNDARY FRAME EXPANSION: A DERIVATION OF UNRESTRAINED BEAM-GROWTH

A widespread concern with the practical implementation of self-centering frames with HBE-to-VBE rocking connections is the issue of "beam-growth" (i.e., frame beam elongation or PT boundary frame expansion). This phenomenon occurs because the joint opening at each end of the beam (which is required in order to induce PT tensile strains for recentering) manifests itself as an apparent increase in horizontal length of the beams (although physically the beam length remains essentially the same). This has the undesired effect of the beams pushing outward against the columns by the amount of the gap openings at the beam-to-column rocking joints. As a consequence, strength demands on the columns are increased (i.e., columns must flexurally deform to accommodate the beam growth) as well as strain compatibility issues of the diaphragm connection to the beams arise (i.e., the diaphragm must slip/tear or deform to accommodate the beam growth).

Large-scale experimental investigation (Dowden and Bruneau, 2014; Dowden et al., 2016) of a single-bay, two-story NZ-SC-SPSW showed that even though the NewZ-BREAKSS rocking connection was proposed to eliminate beam-growth effects, a small but observable amount of beam growth does develop for the NewZ-BREAKSS rocking connection, contrary to what was initially assumed (insignificant compared to connections rocking about their top and bottom HBE flanges but, nonetheless, required to be understood). As a result of this observation, closer scrutiny of the kinematics of this connection has lead to a better understanding of beam growth; equations that could be used to inform design and optional modifications to the NewZ-BREAKSS detail to completely eliminate beam-growth effects are presented.

The analytical relationship for unrestrained beam growth can be obtained by reviewing the free-body diagram shown in Figure 20 and observing that, for the rightward drift shown in that figure, the rotation at the left and right VBE differ by an incremental amount $\Delta\theta$ as a result of beam growth, where the additional parameters in the figure are defined as follows:

θ = VBE rotation at a known drift level

$h1$ = height from the VBE base to the bottom most rocking contact point of interest

L_{HBE} = length of the HBE

$\Delta L1$ = horizontal length due to drift rotation θ

$\Delta L2$ = horizontal length due to the drift gap opening θ at the opening joint

d_{VBE} = depth of the VBE, which is shown in a position before and after rotation of the VBE

$D1$ = flange rocking depth rotation lever arm

ΔV, $\Delta H1$ and $\Delta H2$ = incremental dimensions dependent on the VBE base rotation at the VBE location effected by $\theta + \Delta\theta$

x = length parameter used to define $\theta + \Delta\theta$ for subsequent derivation

From the parameters defined, the quantity $\Delta H2$ is the key parameter needed to define the real relationship of unrestrained beam growth (for the conditions noted later) and represents the change in length reduction in the bottom of the parallelogram (indicated in Figures 20 and 21) that takes into account the VBE base rotation $\theta + \Delta\theta$.

Note that the subsequent derivation is based on using a two-story frame with NewZ-BREAKSS rocking connections for illustration purposes. However, the formulations can be applied to a frame of any height and any rocking connection because (1) the height just above ground level controls the kinematic equations, and (2) the parameter associated with the type of rocking connection affecting beam growth is only dependent on the depth of the rocking point rotation lever arm. Furthermore, in this analytical approach, the following simplifications and assumptions was made: (1) The boundary frame is taken as rigid members; (2) the rocking contact points are at the extreme edge of the HBE-to-VBE flange bearing point shown by the "Rocking Contact Point" indicated in Figure 20; (3) local deformation effects at the rocking contact points are neglected; (4) elevation of the HBEs remain unchanged for a given VBE rotation during drift; (5) the HBE-to-VBE joints are frictionless and no PT clamping force is present, allowing the joint to rotate and move freely; and (6) at each VBE location, the line created by joining the points of HBE flange rocking and VBE base rocking points are parallel to the longitudinal axis of the associated VBE.

The formulation of a relationship for unrestrained beam growth first requires the development of an equation for the incremental VBE rotation $\Delta\theta$. This proceeds by first obtaining all of the incremental dimensions at the base of the affected VBE shown in the close-up detail in Figure 20. It

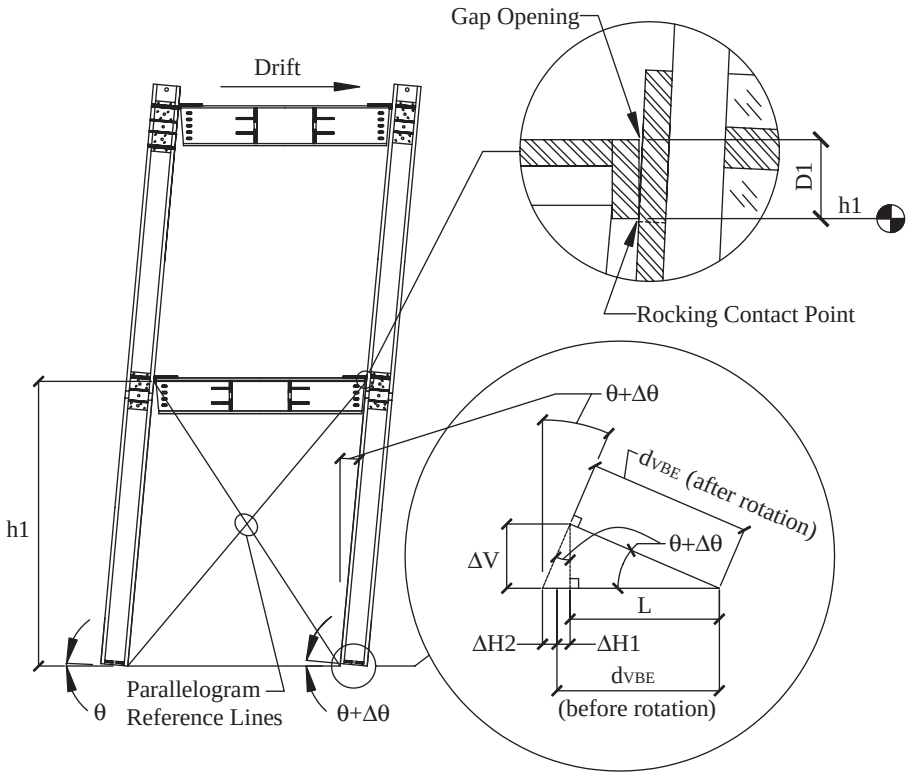

Fig. 20. Frame beam-growth kinematics: free-body diagram 1.

then follows, from geometry, that the vertical displacement at the VBE flange due to rotation is:

$$\Delta V = d_{VBE}\left[\sin(\theta+\Delta\theta)\right] \tag{42}$$

Next, the length of the horizontal projection of the base of the rotated VBE is found to be:

$$L = d_{VBE}\left[\cos(\theta+\Delta\theta)\right] \tag{43}$$

The additional unknown parameter needed to completely define the kinematics at the base of the VBE is ΔH. Derivation of the expression for this term is done in three steps. First, ΔH is equal to the sum of $\Delta H1$ and $\Delta H2$ such that:

$$\Delta H = \Delta H1 + \Delta H2 \tag{44}$$

Second, expanding Equation 44 into an expression in terms of tanθ shown directly in Figure 20 leads to:

$$\Delta H = (\Delta V)\left[\tan(\theta+\Delta\theta)\right] \tag{45}$$

Third, substituting Equation 42 into Equation 45 leads to:

$$\Delta H = d_{VBE}\left[\tan(\theta+\Delta\theta)\sin(\theta+\Delta\theta)\right] \tag{46}$$

Toward derivation of an expression for Δθ, the horizontal projection of the base of the rotated VBE extending beyond the footprint of the VBE prior to rotation needs to be established (i.e., $\Delta H2$), which can be calculated as:

$$\begin{aligned}\Delta H2 &= (\Delta H + L) - d_{VBE}\\ &= d_{VBE}\left[\tan(\theta+\Delta\theta)\sin(\theta+\Delta\theta)+\cos(\theta+\Delta\theta)-1\right]\end{aligned} \tag{47}$$

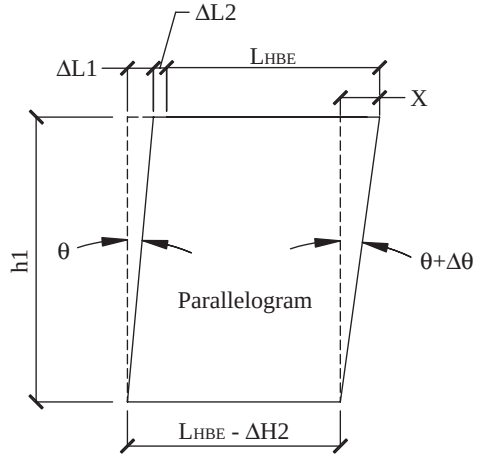

Fig. 21. Frame beam-growth kinematics: free-body diagram 2.

Additionally, the inside surface of the deformed frame displacement can be bounded by a parallelogram from which the geometry θ + Δθ can be determined and from which Δθ can then be calculated for any known value of θ (i.e., typically by selecting a target drift). From the free-body diagram of the parallelogram in Figure 21 for all remaining derivation steps, begin with defining the horizontal length due to frame drift as:

$$\Delta L1 = h1(\tan\theta) \tag{48}$$

The incremental horizontal length due to HBE-to-VBE gap opening is:

$$\Delta L2 = D1(\tan\theta) \tag{49}$$

Next, solving for tan(θ + Δθ), and substituting Equations 47, 48 and 49 for $\Delta H2$, $\Delta L1$ and $\Delta L2$, respectively, into Equation 50 leads to:

$$\begin{aligned}\tan(\theta+\Delta\theta) &= \frac{x}{h1}\\ &= \frac{(\Delta L1+\Delta L2+L_{HBE})-(L_{HBE}-\Delta H2)}{h1}\\ &= \frac{\Delta L1+\Delta L2+\Delta H2}{h1}\\ &= \frac{(h1+D1)\left[\tan(\theta)\right]+d_{VBE}\left[\tan(\theta+\Delta\theta)\sin(\theta+\Delta\theta)+\cos(\theta+\Delta\theta)-1\right]}{h1}\end{aligned} \tag{50}$$

Solving Equation 50 for tan(θ) leads to the following relationship defining unrestrained beam growth:

$$\tan(\theta) = \frac{\tan(\theta+\Delta\theta)\left\{h1-d_{VBE}\left[\sin(\theta+\Delta\theta)\right]\right\}+d_{VBE}\left[1-\cos(\theta+\Delta\theta)\right]}{h1+D1} \tag{51}$$

In this equation, all parameters have been defined previously and are known except for Δθ. One approach to solve Equation 51 consists of iterating on the value of Δθ until convergence. Once the parameter Δθ is known, the beam growth at each floor level can then be calculated.

Although the solution for Δθ will converge fairly quickly, an alternate simplified formulation can be used that provides an approximate solution without iteration. This is obtained by realizing that the reduction in length of the bottom of the parallelogram due to $\Delta H2$ (from the VBE base rotation) is insignificant. The procedure then follows by letting $\Delta H2 = 0$ in the preceding derivation; thus, the expression for tan(θ + Δθ) simplifies to:

$$\tan(\theta+\Delta\theta) \cong \frac{h1+D1}{h1}\left[\tan(\theta)\right] \tag{52}$$

Given the insignificance of $\Delta H2$, the approximate solution to obtain $\Delta\theta$ using Equation 52 will be within a percent accuracy compared to that using the exact relationship shown in Equation 51 that requires more computational effort. Once $\Delta\theta$ is known, the calculation of beam-growth demand at each level can be obtained. To illustrate the calculation of beam growth and the distribution along the frame height, using the frame shown in Figure 20 as an example, the calculations are made with the following assumptions:

- The story heights at each level are equal to h.
- The rocking depth at HBE level 1 and 2, respectively, is $D1 = D2 = D$.
- The height to the bottom gap opening $h1$ is equal to h to keep calculations simple for illustration purposes. This will lead to an approximate solution because $h1$ at the ground level is actually $h1 = h - D$ if story heights are equal.

The following calculations are then made:

Step 1 Calculate the gap adjustment $\delta = (\Delta\theta)(h1)$ due to beam-growth at the level 1 HBE. Because the adjustment is required at the level 1 HBE, the bottom of flange gap opening is zero (i.e., in bearing contact with the VBE flange). The top of flange gap opening is equal to $(D)(\theta + \Delta\theta)$.

Step 2 Calculate the gap openings at the roof HBE. The bottom of flange gap is equal to $(\Delta\theta)(2h)$; this represents the incremental gap opening required due to beam-growth. The top of flange gap is equal to $(\Delta\theta)(2h) + (\theta + \Delta\theta)(D)$; the first component represents the incremental gap opening required due to beam growth (also is the gap opening at the bottom of flange), and the latter component is the gap opening due to the joint rotation.

Note that if additional stories were present, beam-growth at each subsequent level would increase proportionally to the height of the bottom of flange level at that location only. For example, if there was an additional floor level in the example shown, the bottom of the flange gap would be equal to $(\Delta\theta)(3h)$ and the top of flange gap would be equal to $(\Delta\theta)(3h) + (\theta + \Delta\theta)(D)$. That is, the component due to the gap opening due to the joint rotation remains constant, and only the incremental gap opening due to beam growth increases with story height. Furthermore, to capture the beam-growth behavior about the top flange in the numerical model response, an alternate (but more complex) HBE-to-VBE model presented by Dowden and Bruneau (2014) would be required.

Two alternative modifications to the original proposed NewZ-BREAKSS rocking flange detail (Dowden and Bruneau, 2011) are proposed to eliminate the effects due to beam growth observed in the referenced large-scale NZ-SC-SPSW test. The first modification is to provide a semispherical bearing bar plate at the end of the HBE flange and reinforcement plates, as shown in Figure 22a. The second option is to provide both a semispherical bearing bar plate and additional PT elements near the bottom of the top flange, as shown in Figure 22b; these latter supplemental PT elements would be designed to always remain in tension. Although the first alternative should eliminate beam-growth effects, the latter option would further enhance the performance of the NewZ-BREAKSS connection and would also provide some increase in the recentering potential of the PT boundary frame.

SUMMARY AND CONCLUSIONS

Self-centering steel plate shear walls having NewZ-BREAKSS connections (i.e., NZ-SC-SPSW) are an alternative lateral-force-resisting system to conventional steel plate

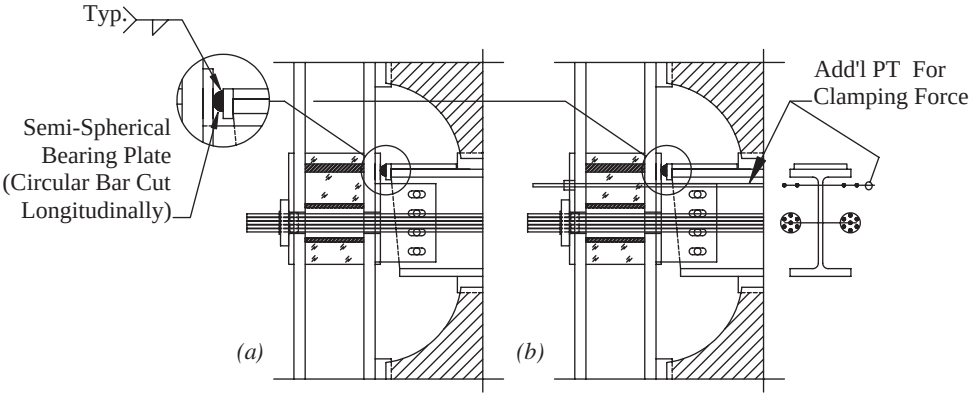

Fig. 22. Modified NewZ-BREAKSS detail: (a) alternative 1; (b) alternative 2.

shear walls for buildings located in regions of high seismicity. In this paper, the fundamental kinematic behavior of the NZ-SC-SPSW has been established. Closed-form solutions equations were derived for (1) HBE strength demands along the HBE based on capacity design principles, (2) infill web plate strains for HBE-to-VBE rocking joints, and (3) unrestrained beam growth with frames with rocking joints susceptible to beam-growth effects. Additionally, numerical models for the NewZ-BREAKSS connection using the programs SAP2000 and OpenSees were presented. Furthermore, nonlinear pushover analyses were conducted to validate the derived HBE strength demand equations and to provide insight on the effects of the PT on base shear versus roof drift frame response. The equations and free-body diagrams presented not only provide insight on the behavior of the NZ-SC-SPSW system, but also inform design. Furthermore, a modified NewZ-BREAKSS connection is proposed to eliminate beam-growth effects observed from recent large-scale tests (Dowden and Bruneau, 2014; Dowden et al., 2016).

ACKNOWLEDGMENTS

Financial support for this study was provided by the National Science Foundation as part of the George E. Brown Network for Earthquake Engineering Simulation under award number CMMI-0830294. Additional financial support for D. Dowden was provided by MCEER. Any opinions, findings, conclusions and recommendations presented in this paper are those of the authors and do not necessarily reflect the views of the sponsors.

REFERENCES

AIJ (1995), "Performance of Steel Buildings During the 1995 Hyogoken–Nanbu Earthquake," Tokyo: Architectural Institute of Japan. (In Japanese with English summary).

AISC (2010), *Seismic Provisions for Structural Steel Buildings,* ANSI/AISC 341-05, American Institute of Steel Construction, Chicago, IL.

Berman, J. and Bruneau, M. (2008), "Capacity Design of Vertical Boundary Elements in Steel Plate Shear Walls," *Engineering Journal*, AISC, Vol. 45, No. 1, 1st Quarter, pp. 57–71.

Christopoulos, C., Filiatrault, A., Uang, C.M. and Folz, B. (2002), "Posttensioned Energy Dissipating Connections for Moment-Resisting Steel Frame," *Journal of Structural Engineering*, ASCE, Vol. 128, No. 9, pp. 1,111–1,120.

Christopoulos, C., Pampanin, S. and Priestley, M.J.N. (2003), "Performance-Based Seismic Response of Frame Structures Including Residual Deformations. Part I: Single-Degree of Freedom Systems," *Journal of Earthquake Engineering*, Vol. 7, No. 1, pp. 97–118.

Clayton, P.M. (2013), "Self-Centering Steel Plate Shear Wall: Subassembly and Full-Scale Testing," Ph.D. dissertation, Department of Civil and Environmental Engineering, University of Washington, Seattle, WA.

Clayton, P.M., Berman, J.W. and Lowes, L.N. (2012), "Seismic Design and Performance of Self-Centering Steel Plate Shear Walls," *Journal of Structural Engineering*, ASCE, Vol. 138, No. 1, pp. 22–30.

Clifton, G.C. (1996), "Development of Perimeter Moment-Resisting Steel Frames Incorporating Semi-Rigid Elastic Joints," *Proc. New Zealand National Society for Earthquake Engineering Conference*, pp. 177–184.

Clifton, G.C. (2005), "Semi-Rigid Joints for Moment Resisting Steel Framed Seismic Resisting Systems," Ph.D. dissertation, Department of Civil and Environmental Engineering, University of Auckland, New Zealand.

Clifton, G.C., MacRae, G.A., Mackinven, H., Pampanin, S. and Butterworth, J. (2007), "Sliding Hinge Joints and Subassemblies for Steel Moment Frames," *Proc. New Zealand Society of Earthquake Engineering Annual Conference,* Paper 19, Palmerston North, New Zealand.

CSI (2009), "SAP2000: Static and Dynamic Finite Element Analysis of Structures (Version 14.1.0)," Computers and Structures Inc., Berkeley, CA.

Dowden, D.M. (2014), "Resilient Self-Centering Steel Plate Shear Walls," Ph.D. dissertation, Department of Civil and Environmental Engineering, University at Buffalo, Buffalo, NY.

Dowden, D.M. and Bruneau, M. (2014), "Analytical and Experimental Investigation of Self-Centering Steel Plate Shear Walls," *Technical Report MCEER-14-0010*, Multidisciplinary Center for Earthquake Engineering Research, State University of New York Buffalo, Buffalo, New York.

Dowden, D.M., Clayton, P.M., Li, C.-H., Berman, J.W., Bruneau, M, Lowes, L.N. and Tsai, K.C. (2016), "Full-Scale Pseudo-Dynamic Testing of Self-Centering Steel Plate Shear Walls," *Journal of Structural Engineering*, ASCE, Vol. 142, No. 1, doi: 10.1061/(ASCE) ST.1943-541X.0001367.

Dowden, D.M. and Bruneau, M. (2011), "NewZ-BREAKSS: Post-Tensioned Rocking Connection Detail Free of Beam Growth," *Engineering Journal*, AISC, Vol 48, No. 2, 2nd Quarter, pp. 153–158.

Dowden, D.M., Purba, R. and Bruneau, M. (2012),"Behavior of Self-Centering Steel Plate Shear Walls and Design Considerations." *Journal of Structural Engineering*, ASCE, Vol. 138, No. 1, pp. 11–21.

Garlock, M. (2002), "Design, Analysis, and Experimental Behavior of Seismic Resistant Post-Tensioned Steel Moment Frames," Ph.D. dissertation, Department of Civil and Environmental Engineering, Lehigh University, Bethlehem, PA.

Garlock, M., Ricles, J. and Sause, R. (2005), "Experimental Studies of Full-Scale Posttensioned Steel Connections," *Journal of Structural Engineering*, ASCE, Vol. 131, No. 3, pp. 438–448.

Kawashima, K., MacRae, G.A., Hoshikuma, J.-I. and Nagaya, K. (1998), "Residual Displacement Response Spectrum," *Journal of Structural Engineering*, ASCE, Vol. 124, No. 5, pp. 523–530.

Krawinkler, H., Anderson, J., Bertero V., Holmes, W. and Theil, C., Jr. (1996), "Steel Buildings," *Earthquake Spectra,* Vol. 12, No. S1, pp. 25–47.

MacRae, G.A., Clifton, G.C., Mackinven, H., Mago, N., Butterworth, J. and Pampanin, S. (2008), "The Sliding Hinge Joint Moment Connection," *Bulletin of the New Zealand Society for Earthquake Engineering,* Vol. 43, No. 3, pp. 202–212.

Mazzoni, S., McKenna, F., Scott, M.H. and Fenves, G.L. (2009), "Open System for Earthquake Engineering Simulation User Command-Language Manual—OpenSees Version 2.0," Pacific Earthquake Engineering Research Center, University of California, Berkeley, Berkeley, CA.

Pampanin, S., Christopoulos, C. and Priestley, M.J.N. (2003), "Performance-Based Seismic Response of Frame Structures Including Residual Deformations. Part II: Multi-Degree of Freedom Systems," *Journal of Earthquake Engineering*, Vol. 7, No. 1, pp. 119–147.

Ricles J.M., Sause R., Peng, S. and Lu, L. (2002), "Experimental Evaluation of Earthquake Resistant Posttensioned Steel Connections," *Journal of Structural Engineering*, ASCE, Vol. 128, No. 7, pp. 850–859.

Rojas, P., Ricles, J.M. and Sause, R. (2005), "Seismic Performance of Post-Tensioned Steel Moment Resisting Frames with Friction Devices," *Journal of Structural Engineering*, ASCE, Vol. 131, No. 4, pp. 529–540.

Sabelli, R. and Bruneau, M. (2007), *Steel Plate Shear Walls*, Design Guide 20, AISC, Chicago, IL.

Webster, D.J. (2013), "The Behavior of Unstiffened Steel Plate Shear Wall Web Plates and Their Impact on the Vertical Boundary Elements," Ph.D. dissertation, Department of Civil and Environmental Engineering, University of Washington, Seattle, WA.

Winkley, T.B. (2011), "Self-Centering Steel Plate Shear Walls: Large Scale Experimental Investigation," M.S. thesis, Department of Civil and Environmental Engineering, University of Washington, Seattle, WA.